Raman Studies of Carbon Nanostructures

Ado Jorio[1] and Antonio G. Souza Filho[2]

[1]Departamento de Física, Universidade Federal de Minas Gerais, Belo Horizonte, MG 31270-901, Brazil; email: adojorio@fisica.ufmg.br

[2]Departamento de Física, Universidade Federal do Ceará, Fortaleza, CE 60455-900, Brazil; email: agsf@fisica.ufc.br

Keywords

Raman spectroscopy, graphene, carbon nanotubes, carbyne, charcoal

Abstract

This article reviews recent advances on the use of Raman spectroscopy to study and characterize carbon nanostructures. It starts with a brief survey of Raman spectroscopy of graphene and carbon nanotubes, followed by recent developments in the field. Various novel topics, including Stokes–anti-Stokes correlation, tip-enhanced Raman spectroscopy in two dimensions, phonon coherence, and high-pressure and shielding effects, are presented. Some consequences for other fields—quantum optics, near-field electromagnetism, archeology, materials and soil sciences—are discussed. The review ends with a discussion of new perspectives on Raman spectroscopy of carbon nanostructures, including how this technique can contribute to the development of biotechnological applications and nanotoxicology.

1. INTRODUCTION

This article reviews the use of Raman spectroscopy for the development of science and technology in carbon-based nanomaterials, with a focus on graphene and carbon nanotubes. Raman spectroscopy relies on the modulation of materials polarizability by phonons or by any other excitation in the material, and here resides the power of the technique when applied to carbon structures. It is well established that Raman spectroscopy is a very powerful tool for studying carbon nanostructures (1–8). For every newly discovered carbon nanomaterial and every novel application of a carbon nanostructure, Raman spectroscopy can be used as a characterization tool, either revealing new properties or simply proving the presence of a desired structure or functionalization. In addition to Raman scattering in carbon materials being generally strong compared with the same effect in other materials, complex resonant electron-phonon and electron-light interactions take place, thus enriching the phenomena and the outcomes of related studies.

From the materials perspective, the unusually high strength of the carbon-carbon bonds generates different nanostructures with enough stability to serve as prototype materials for the development of nanoscience and nanotechnology (1, 2, 9, 10). Graphene can be gradually ion bombarded and subsequently tested, demonstrating its evolution from a perfect hexagonal structure to an amorphous material (11). The amorphous material can be a model for the study of charcoal-like structures, which are important not only in materials science, but also in archeology and soil sciences (12, 13). Graphene can be folded to generate superlattices with tunable electronic structures (14–16). Such structures can be used to study new phenomena, such as the generation of quantum-optical memories based on Stokes and anti-Stokes inelastic light scattering (17). Carbon nanotubes can be used as a delivery agent for RNA transfection into different environments (18, 19). When RNA is inserted into living cells, this transfection procedure can be used as a genetic therapy (20). Carbon nanotubes can serve as a shield for the study of perfect one-dimensional carbon chains under high pressure, although such a structure would be unstable in free space (21). Graphene and carbon nanotubes can be used as probes to study near-field electromagnetic phenomena in well-designed plasmonic micro- and nanostructures (22–24). All these are examples of the advantage of using Raman spectroscopy and carbon nanostructures for the development of nanoscience and nanotechnology.

The review is structured as follows. Section 2 describes the basic aspects that are already established in the field. This description is brief because there are several Raman spectroscopy reviews devoted to graphene (Section 2.1) and carbon nanotubes (Section 2.3), including disorder effects in graphene-like structures (Section 2.2) (1–8). The sections that follow address new phenomena, such as Stokes–anti-Stokes correlation (Section 3), the development of tip-enhanced Raman spectroscopy (TERS) in two dimensions (Section 4), the use of high pressure (Section 5) to study separately the inner and outer walls in double-wall carbon nanotubes (DWCNTs) (Section 5.1) and triple-wall carbon nanotubes (TWCNTs) (Section 5.2), and strain effects in one-dimensional carbon chains inside nanotubes and thus shielded from the environment (Section 5.3). Finally, the review presents a perspective section (Section 6) that discusses (*a*) future directions for the new phenomena discussed here (Section 6.1) and (*b*) applications of Raman on nanocarbon in other fields (Section 6.2), including biotechnology (Section 6.2.1), nanotoxicology (Section 6.2.2), and archeology and soil sciences (Section 6.2.3).

2. BASICS OF RAMAN SPECTROSCOPY IN GRAPHENE AND CARBON NANOTUBES

Figure 1 exhibits the Raman spectra of different carbon nanostructures. The similarities of and differences between the spectra enable one to identify the different carbon structures and to study their properties in great detail.
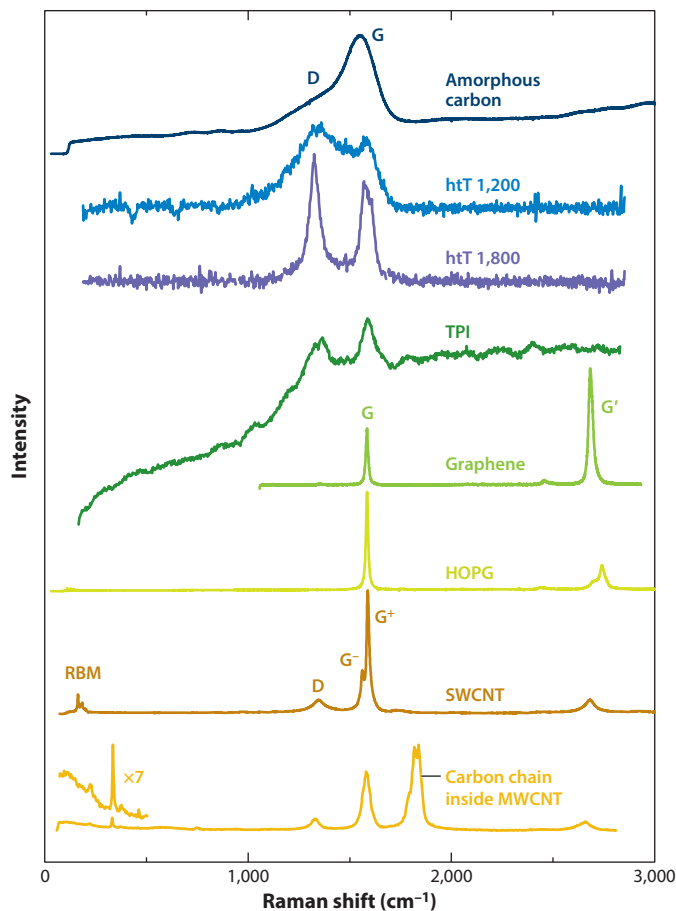
Figure 1

Raman spectra of different graphene-based systems. From top to bottom: as-produced amorphous carbon, amorphous carbon heat treated at 1,200°C (htT 1,200) and at 1,800°C (htT 1,800), charcoal grains from the Terra Preta do Índio (TPI), single-layer graphene, highly ordered pyrolytic graphite (HOPG), single-wall carbon nanotube (SWCNT) bundles, and multiwall carbon nanotube (MWCNT) bundles filled with linear carbon chains. The different Raman peaks discussed in the text are labeled. RBM denotes radial breathing mode.

2.1. Graphene

Monolayer graphene (the fourth spectrum from the bottom in **Figure 1**) exhibits a hexagonal symmetry belonging to the space group $P6/mmm$ (D_{6h}^1) (25). With two inequivalent carbon atoms in the unit cell, the phonon dispersion has six phonon branches (2, 6, 8). At the center of the Brillouin zone (Γ point, wave vector $q = 0$), the wave vector group is isomorphic to the point group D_{6h}, with only one first-order Raman active mode (named the G band), belonging to the double-degenerate irreducible representation E_{2g}, appearing at 1,584 cm^{-1} (8). The relatively high frequency of this optical phonon (approximately 0.2 eV) is due to the light weight of the carbon atoms ($Z = 6$) and to the high stiffness of the carbon-carbon σ bonds. For this reason, Raman spectroscopy can be used to probe relatively small environmental perturbations, including variations in strain, doping, and temperature, because these perturbations change the G band frequency by a measurable quantity (8). A Kohn anomaly effect makes the G band frequency

highly sensitive to changes in the Fermi level (26). Perturbations may lead to symmetry breaking that can also be measured with Raman spectroscopy (25). Interestingly, the structure of other two-dimensional materials, such as phosphorene, silicene, and germanene, can be achieved by continuous symmetry changes to the graphene structure (27).

Besides the first-order Raman-allowed G band, graphene exhibits other Raman features that are related to phonons in the interior of the Brillouin zone, which are activated by resonant electron-phonon scattering (28, 29). The most prominent is the second-order G′ band, appearing at approximately 2,700 cm^{-1} and generated by two phonons belonging to the in-plane transversal optical (iTO) phonon near the K point in the Brillouin zone (8). This specific phonon exhibits strong electron-phonon coupling, thus generating the strong G′ band (30), although all the other phonon branches in graphene can generate similar scattering events, and several small peaks are observed in the graphene Raman spectra (28, 29, 31). These same phonons can be observed in a first-order scattering process involving only one phonon, but in this case graphene has to contain defects to activate the first-order scattering event from $q \neq 0$ phonons (29, 32, 33). The most prominent band is again the iTO phonon near the K point, showing up at approximately 1,350 cm^{-1}; it is named the D band to account for its relation to defects (present in several spectra in **Figure 1**). Notice that for the Raman shift (cm^{-1}) G′ ≈ 2 D (8), and this feature is further discussed in Section 2.2. One interesting aspect of these resonant electron-phonon scattering processes is that the resonant phonon wave vector depends on the excitation laser energy, and the D and G′ Raman peaks change frequency when changing laser energy (28, 29, 31).

Graphene can be stacked to form multilayer graphene; the most common stacking order is referred to as Bernal or AB stacking (1, 2, 9). If AB stacking applies and N is denoted as the number of layers, the symmetry of the system is the same if N is even or odd, regardless of the absolute value of N, except for the cases of monolayer graphene ($N = 1$) and graphite ($N \rightarrow \infty$; third spectrum from the bottom in **Figure 1**), which have their unique symmetries (25). The main symmetry operations distinguishing the point groups between even-N and odd-N graphene are the horizontal mirror plane and the inversion center. At the Γ point, the point group is D_{3d} when N is even and D_{3h} when N is odd.

Besides the in-plane vibrations, such as the D, G, and G′ (2D) bands, there are interlayer vibrations when $N > 1$, and these vibrations are related to the coupling of two or more layers (34, 35). The frequencies of these interlayer vibrations are generally much lower than those for the in-layer vibrations because the interlayer coupling in two-dimensional materials is due to weak van der Waals forces. The physics of interlayer vibrations is general for two-dimensional materials with two layers or more, as it is independent of the specific symmetry of the two-dimensional lattice. There are two main sets of interlayer vibrations, shear and breathing between two adjacent layers, and their frequencies and number of modes depend on the number of layers (36).

Because N-layer graphene has $2N$ atoms in the unit cell, the number of phonon branches will be multiplied by N. For this reason, Raman spectroscopy can be used to assign the number of layers in a graphene sample. The in-plane G′-related vibration is the most commonly used vibration for this purpose (25, 30, 37). Interlayer vibrations can also be used to identify N because their mode frequencies depend on N (34, 35). The drawbacks here are that their frequencies are usually very low, so special filters are needed in the setup for their experimental observation.

Finally, there are other stacking arrangements named AA, ABC, and so on (1, 2, 9). One arrangement that deserves special attention is so-called twisted bilayer graphene, in which neighboring graphene sheets are twisted with respect to each other at an arbitrary angle θ (14–16). Such a twist generates superlattices that can activate phonons from the interior or the Brillouin zone, which are observed in their Raman spectra (38–40). The activated phonons depend on θ,

and such a system has been used to measure the phonon dispersion of graphene (41). Conversely, the Raman frequencies of the activated modes are used to identify θ.

2.2. Disorder in Graphene Systems

The disorder-induced D band appears when there are defects in the perfectly hexagonal sp^2 network. **Figure 1** shows the D band for as-produced amorphous carbon (top spectrum), for amorphous carbon heat treated at 1,200°C (second spectrum from the top), and for amorphous carbon heat treated at 1,800°C (third spectrum from the top). Notice the change in relative intensities and width for the D and G bands, which drive the use of Raman spectroscopy to characterize the sp^2 ordering in those structures. **Figure 1** also shows the D band for a charcoal grain found in an Amazonian soil [Terra Preta de Índio (TPI), fourth spectrum from the top], and this subject is discussed in Section 6.2.3. The two carbon nanotubes spectra shown in **Figure 1** (bottom and second-to-bottom spectra) exhibit a small D peak, indicating that these carbon nanotube samples have some defects in their walls. The graphene and highly ordered pyrolytic graphite spectra (third and fourth spectra from the bottom) show no D peak, indicating high crystallinity.

The observation of the disorder-induced D band is related to defects in the sp^2 carbon lattice, and the ratio between the D and G band intensities (I_D/I_G) has been broadly used to quantify disorder in nanostructured graphitic samples (11, 32, 33, 42–45). I_D/I_G can be used to quantify both point defects, like vacancies or dopant atoms (11, 44), and crystallite borders in a multidomain graphene sample (43, 45). Although the physics underlying the scattering effects is the same, the dependence on the amount of disorder differs because point defects are zero-dimensional local symmetry breaking of the graphene periodicity, whereas crystallite borders are one-dimensional structures (11, 45).

Ready-to-use equations are valid for different ranges due to the different geometrical aspects. In the case of nanostructured graphene crystallites with average sizes (L_a) larger than the phonon coherence length, i.e., $L_a > 30$ nm (43, 45),

$$\frac{I_D}{I_G} = \frac{(2.4 \times 10^{-10})\lambda_L^4}{L_a}, \qquad 1.$$

where λ_L is the excitation laser wavelength. Both λ_L and L_a are given here in nanometers. For samples with point defects separated by an average distance among defects L_D (11, 44),

$$\frac{I_D}{I_G} = \frac{(1.8 \times 10^{-9})\lambda_L^4}{L_D^2}. \qquad 2.$$

Again, λ_L and L_D are given in nanometers. Equation 2 holds for $L_D > 10$ nm, because L_D is not directly related to the phonon confinement length in the case of point defects.

These equations have been used to quantify the low density of defects in graphene-like materials, including carbon nanotube length, because the tube ends here are seen as the defects (46). However, for $L_a < 30$ nm or $L_D < 10$ nm, the I_D/I_G ratio is not a well-defined figure of merit to quantify disorder, and the phonon line width, which is tightly related to phonon confinement, becomes more appropriate. In these lower limits, the G band full width at half-maximum (FWHM) is given by either (45, 47)

$$\Gamma_G = 15 + 95e^{\frac{-2L_a}{32}} \qquad 3.$$

or

$$\Gamma_G = 15 + 95e^{\frac{-2L_D}{10}}. \qquad 4.$$

In Equations 3 and 4, Γ_G is in units of cm^{-1}, and L_a and L_D are in nanometers. Examples of the use of these equations in archeology and soil sciences are given in Section 6.2.3.

2.3. Carbon Nanotubes

Carbon nanotubes (bottom and second-to-bottom spectra in **Figure 1**) are more complex than graphene because they exhibit an infinity of possible diameters (d_t) and chiral angles (θ). A specific nanotube is indexed by a pair of indices (n, m). Moreover, when the discussion moves from graphene to carbon nanotubes, the curvature, the symmetry, and the quantum confinement of both electrons and phonons along the circumference of the tube (whose length is only approximately 1 nm) bring subtleties to their Raman spectra; such subtleties have been extensively used for advancing the physics of nanotubes (2, 6, 8). The symmetry aspects, including the Raman selection rules of carbon nanotubes, were summarized in Reference 48.

Quantum confinement is responsible for the appearance of one-dimensional van Hove singularities in the density of electronic states in the valence and conduction bands (2) and for strong many-body effects (49). Each nanotube has a unique set of sharp optical transitions, usually named E_{ii} (i is a level index). By choosing the appropriate energy of the excitation light source, it is possible to resonantly excite the Raman spectra of specific nanotubes (50–52). Most theoretical advances made in understanding the optical transition energies for carbon nanotubes were made possible only by accurate (n, m) assignment procedures (53). Well-established guides, including the effect of different environments, were developed for listing the E_{ii} values as a function of (n, m) (54).

As in the context of graphene, the G band, the G′ band, and the disorder-induced D band have been used to study and characterize carbon nanotubes. Understanding from these Raman features was actually developed for carbon nanotubes before the discovery of graphene. The Raman spectra of carbon nanotubes are characterized by a larger number of Raman peaks, which either become Raman active due to the reduced symmetry of the tube or appear because of different resonance processes involving other phonons inside the Brillouin zone. The G band, for example, is multifeatured in carbon nanotubes, and the relative peak frequencies and intensities depend on (n, m). Up to six peaks can be Raman active within the G band, with the most intense termed the G$^+$ (higher-frequency) and G$^-$ (lower-frequency) components. Kohn anomaly effects make an important contribution to the optical phonons in carbon nanotubes and explain several unique features such as the softening (broadening) and hardening (narrowing) of the G band frequency (line width) as a function of Fermi level change, which is most prominent in metallic tubes (8, 26, 55). Strain effects, including ovalization and nanotube collapse, were studied using the evolution of the G band frequency as a function of external pressure (56–62). For peaks that are activated by electron-phonon resonant scattering, like the D and G′ bands, there are differences between graphene and carbon nanotubes due to a selection of k wave vectors related to the k vector location of the one-dimensional van Hove singularities (63).

The most remarkable Raman feature of carbon nanotubes, compared to other sp^2-based carbons, is the existence of the so-called radial breathing mode (RBM), which appears at low energies. This phonon mode is related to the perfectly symmetric expansion and contraction of the tube in the radial direction, and its frequency (ω_{RBM}) shows a diameter dependence. Whereas graphene needs multilayers to exhibit the interlayer breathing-like mode, a single-wall carbon nanotube (SWCNT) is a closed cylinder and exhibits a breathing mode. The RBMs usually appear at higher frequencies than do the graphene multilayer breathing modes, and they have become the spectroscopic signature of nanotubes, with frequency given by

$$\omega_{RBM} = \frac{227}{d_t}\sqrt{1 + C_e d_t^2},$$

5.

where C_e is a fitting parameter used to account for the interaction of the nanotube with its surrounding environment (54, 64–66). In Equation 5, ω_{RBM} is in units of cm^{-1} and d_t is in nanometers.

3. CORRELATION BETWEEN STOKES AND ANTI-STOKES RAMAN SCATTERING

Being related to the annihilation of a phonon in a material, the anti-Stokes Raman scattering intensity is strongly dependent on the phonon population, which is governed by the local temperature (8). On the basis of this property, the anti-Stokes–Stokes intensity ratio (I_{aS}/I_S) has been broadly used to study the phonon population dependence of different properties in graphene and carbon nanotubes, such as thermal conductivity (67), effective temperatures of biased nanostructures (68), electrical power (69), optical transition energies (70), and phonon lifetimes (71). However, the Raman-active optical phonon in graphene (the G band) has a relatively high energy; i.e., it is weakly populated at room temperature. In this case, the anti-Stokes scattering is very weak. Special conditions may be engineered to generate high anti-Stokes photon emission that originates from a correlated phenomenon termed Stokes–anti-Stokes scattering (17, 72, 73). In Stokes–anti-Stokes scattering, the same phonon generated in the Stokes process is annihilated in the anti-Stokes process. When the Stokes–anti-Stokes phenomena are in place, the I_{aS}/I_S ratio is given by (74)

$$\frac{I_{aS}}{I_S} = C \left(\frac{n_0}{n_0 + 1} + C_{SaS} P_L \right),$$ 6.

where the phonon population n_0 is given by the Bose-Einstein distribution function

$$n_0 = \frac{1}{e^{E_q / k_B T} - 1},$$ 7.

with E_q and $k_B T$ being the q-phonon and thermal energies, respectively, and C being a constant that accounts for the optical properties of the system. The term explicitly dependent on the excitation laser power (P_L) accounts for the Stokes–anti-Stokes–correlated scattering. The constant C_{SaS} depends on fundamental constants, such as coupling and decay rates (74), and it measures the importance of the Stokes–anti-Stokes event. Equation 6 is an approximation valid when $n_0 \ll \gamma/\gamma_C$, where γ and γ_C are the decay rates for the scattered photons and phonons, respectively. This approximation is generally valid for high-frequency phonons, like the optical phonons in graphene. If the C_{SaS} is negligibly small, I_{aS}/I_S will reflect the effective phonon temperature through the Bose-Einstein distribution, as the literature usually assumes.

Figure 2 shows the excitation power dependence behavior for I_{aS}/I_S from different graphene samples and for diamond for comparison (75). Most of the graphene samples exhibit an I_{aS}/I_S excitation laser power dependence that is consistent with an increase in the effective phonon temperature induced by laser heating. However, a different behavior is observed when the twisted-bilayer graphene (tBLG) sample is compared. This specific sample was engineered to exhibit resonance with the anti-Stokes photon emission. The data are fit with Equation 6, and the tBLG data are dominated by the Stokes–anti-Stokes term (74). The Stokes–anti-Stokes term is also dominant in the diamond data shown by open circles (73, 74). However, when graphene and diamond are compared, the Stokes–anti-Stokes phenomenon appears in diamond only when ultrahigh intensities from a pulsed laser are used. Whereas experiments have been performed in diamond with ultrafast pulsed lasers to enhance the response of the nonlinear Stokes–anti-Stokes event (73, 76), the observation of dominant Stokes–anti-Stokes event in graphene has been shown using a few-milliwatt continuous-wave laser (17); i.e., this is achievable even with a simple laser pointer (17).
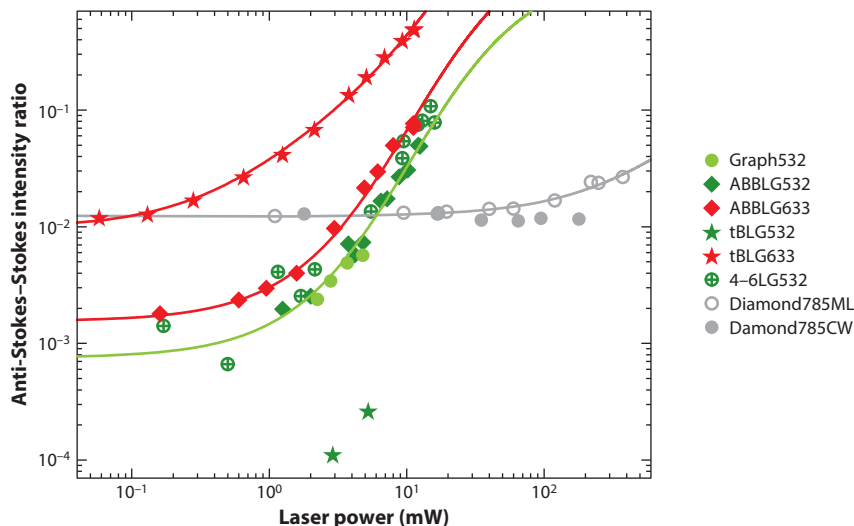
Figure 2

Excitation laser power dependence for the anti-Stokes–Stokes Raman intensity ratio (I_{aS}/I_S) for the different graphene samples (*green* and *red data*) and for diamond (*gray data*) (75). Sample assignments as shown in the legend are as follows: Graph532, single-layer graphene excited at $\lambda = 532$ nm; ABBLG532, AB-stacked bilayer graphene excited at $\lambda = 532$ nm; ABBLG633, AB-stacked bilayer graphene excited at $\lambda = 633$ nm; tBLG532, twisted bilayer graphene excited at $\lambda = 532$ nm; tBLG633, twisted bilayer graphene excited at $\lambda = 633$ nm; 4–6LG532, 4- to 6-layer graphene with AB stacking excited at $\lambda = 532$ nm; Diamond785ML, diamond excited at $\lambda = 785$ nm in the pulsed mode locked regime; Diamond785CW, diamond excited at $\lambda = 785$ nm in the continuous-wave regime. The lines are fitted to the data according with the theory presented in Reference 74.

This correlated Stokes–anti-Stokes scattering has possible applications in quantum information. A solid-state system can work as a quantum memory, storing information in a phonon, between a write (Stokes) procedure and a read (anti-Stokes) procedure (76). The phonon lifetimes in carbon nanostructures are on the order of picoseconds (71), which is enough for thousands of femtosecond optical processing events. The Stokes–anti-Stokes phenomena are also interesting in basic science because the correlated character of the Stokes and anti-Stokes photons can be continuously varied from purely quantum to purely classical regimes regarding phonon population (73). For the optical phonons in both diamond and graphene, the q-phonon energy $E_q \gg k_B T$ at $T \sim 300$ K, and the quantum memory would, in principle, work at room temperature.

4. TIP-ENHANCED RAMAN SPECTROSCOPY IN TWO DIMENSIONS

Raman images can be generated by scanning a nanoantenna (a gold AFM tip) on top of a surface where the nanostructure is sitting, thus generating the TERS effect. The advantage of using near-field optics to image nanostructures is the high localization of the scattering phenomena, with spectral resolution below the diffraction limit (10, 77, 78). TERS with spatial resolution of ~10 nm is established (77), although recent publications indicate TERS resolution on the order of 1 nm (79) or even below (80).

TERS application to graphene-like nanocarbons was initiated with carbon nanotubes (one-dimensional structures) (77, 81), which became a prototype material for the development of TERS (82). Nanoscale vibrational analysis (83), nanoscale optical imaging of excitons (84), TERS
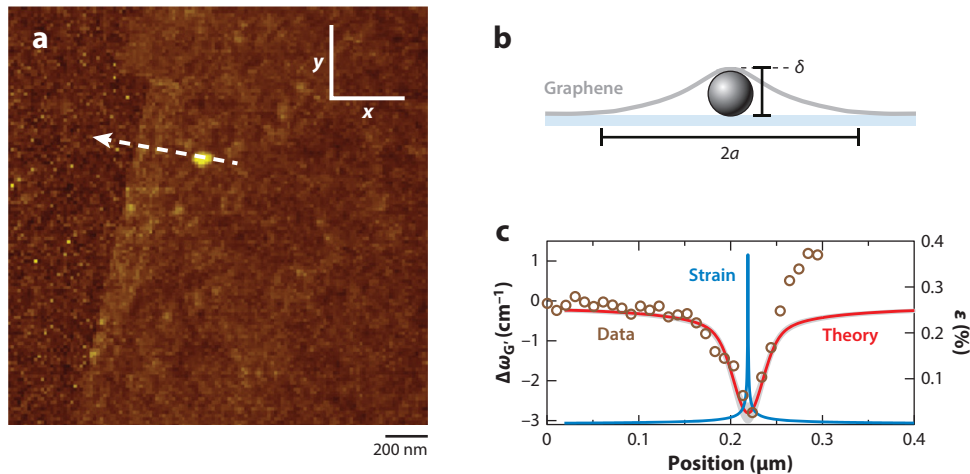
Figure 3

(*a*) AFM image of a graphene flake sitting on a Si substrate. The white arrow indicates the location where a spectral line scan was performed; this location crosses the region where a nanoparticle was covered by the graphene. (*b*) Depiction of a particle straining the graphene locally. (*c*) Plot of the relative Raman shift of the G′ band ($\Delta G'$). By fitting the relative frequency shift (*red line*), the local strain (ϵ, *blue line*) can be extracted. Adapted with permission from Reference 93.

polarization measurements (85), imaging of nanotube chirality changes (86), spectral determination of single charged defects (87), and local optical response of semiconducting nanotubes to DNA wrapping (88) are a few examples of TERS developments using carbon nanotubes.

In the case of graphene (89–95), imaging of defects, contaminants, and crystallite borders is the most common application for TERS. **Figure 3** shows how TERS was used to measure local strain in graphene caused by a small particle under a sheet (93). The strain effect takes place within a 100-nm range; i.e., it would be averaged out if a regular confocal Raman microscope was used.

Graphene was used to study TERS to reveal how the effect takes place in two dimensions. Theory describing the near-field Raman enhancement for two-dimensional systems was developed, and the near-field Raman intensity was quantified as a function of the tip-sample distance (82, 94). The studies considered laser beam configuration, tip orientation relative to the sample, phonon symmetries, and coherence effects. These studies demonstrated that phonon coherence length is an important aspect of the TERS response and that the D, G, and G′ band signals are subjected to different interference effects in the near-field regime, due to their differences in phonon symmetry and dimensionality (95). Analysis of the tip-sample intensity dependence for these three features allowed for indirect measurement of the optical phonon coherence length in graphene, which was found to be $L_C \sim 30$ nm (95). This value sets the limit for phonon confinement effects in nanocrystalline graphene, as discussed in Section 2.2.

5. CARBON NANOTUBE FOR SHIELDING ENVIRONMENT AND HIGH-PRESSURE STUDIES

The empty core of a nanotube is a special environment (on the order of 1 to 2 nm in diameter), perfectly clean and isolated from the surrounding because the nanotube wall is impermeable. These properties—combined with the capillarity effect and the possibility of growing carbon chains, fullerenes, and other nanostructures inside the nanotube during synthesis—have been exploited

for preparing new hybrid materials (96, 97). The outer-tube shell works as a nanotemplate. To probe the structures encapsulated in the nanotubes, optics-based spectroscopy techniques, Raman spectroscopy in particular, are powerful tools because the light is able to excite the inner structures and because the template (outer-tube shell) and the inner structure can be separately characterized in the same experiment. Interactions between these structures also emerge in the spectroscopic response, and both doping and strain can be used to tune and probe the interaction between the encapsulated species and the template.

Strain can be applied to tune the properties of the nanocarbon materials and is suitable for investigating the interaction between a carbon nanotube and its surrounding environment. The multilayer carbon nanotube is an interesting system to be probed under stress because one can study the interaction of the nanotube with another nanotube as the surrounding environment. Hydrostatic pressure combined with Raman spectroscopy has been successfully used for investigating the electronic and mechanical behavior of carbon nanotubes with different numbers of layers (98–102).

5.1. Double-Wall Carbon Nanotubes

DWCNT bundles are easily identified by two separate sets of RBM frequencies that are related to the inner and outer tubes. The pressure response of the inner tube is less pronounced than that of the outer tube, and this difference is due to a screening effect experienced by the outer shell due to the inner tube. At the same time, the collapse of the DWCNTs happens at higher pressures than for SWCNTs with similar nanotube diameters because the inner tube adds mechanical stability to the system (56, 101–103).

The critical pressure for nanotube collapse was probed in pressure-dependent Raman experiments and was shown by a maximum in the ω_G-versus-pressure plot, as shown in **Figure 4** for carbon nanotube with different fillers. The fillers C_{70}, argon, and iodine (104–106) were
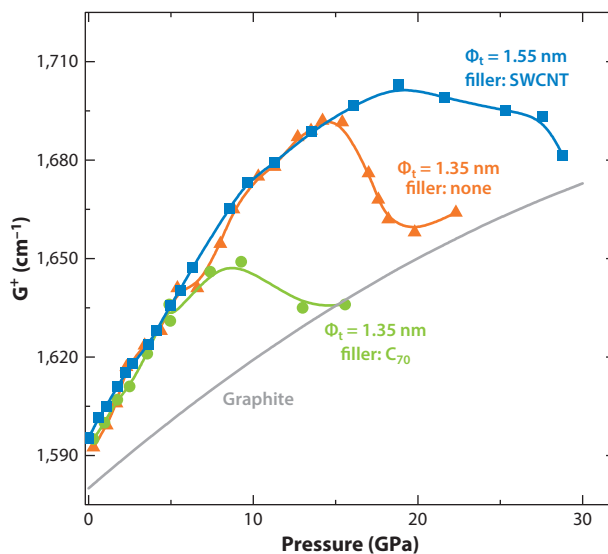
Figure 4

Pressure-dependent G band Raman data (the G^+ component) for nanotubes with different fillers (see legend). Silicone oil was used as the pressure-transmitting medium. The collapse pressure is evidenced by a maximum in the G^+ frequency-versus-pressure curve, which is followed by the G^+ frequency falling down toward the trend exhibited by graphite. SWCNT denotes single-wall carbon nanotube, with Φ_t the average diameter of the tubes. Adapted with permission from Reference 102.

investigated, and the results showed that argon filling leads to an important mechanical stabilization, whereas filling with iodine or C_{70} leads to less stable systems. In the case of DWCNTs, the filling is another nanotube, and the critical collapse pressure is approximately 20 GPa higher than in SWCNTs with the same diameter as the outer DWCNT shell. Because in DWCNTs the outer tube offers chemical screening from the inner tube, whereas the inner tube provides mechanical support to the outer tube, this system is especially interesting for composite nanomaterials, which require high load mechanical support.
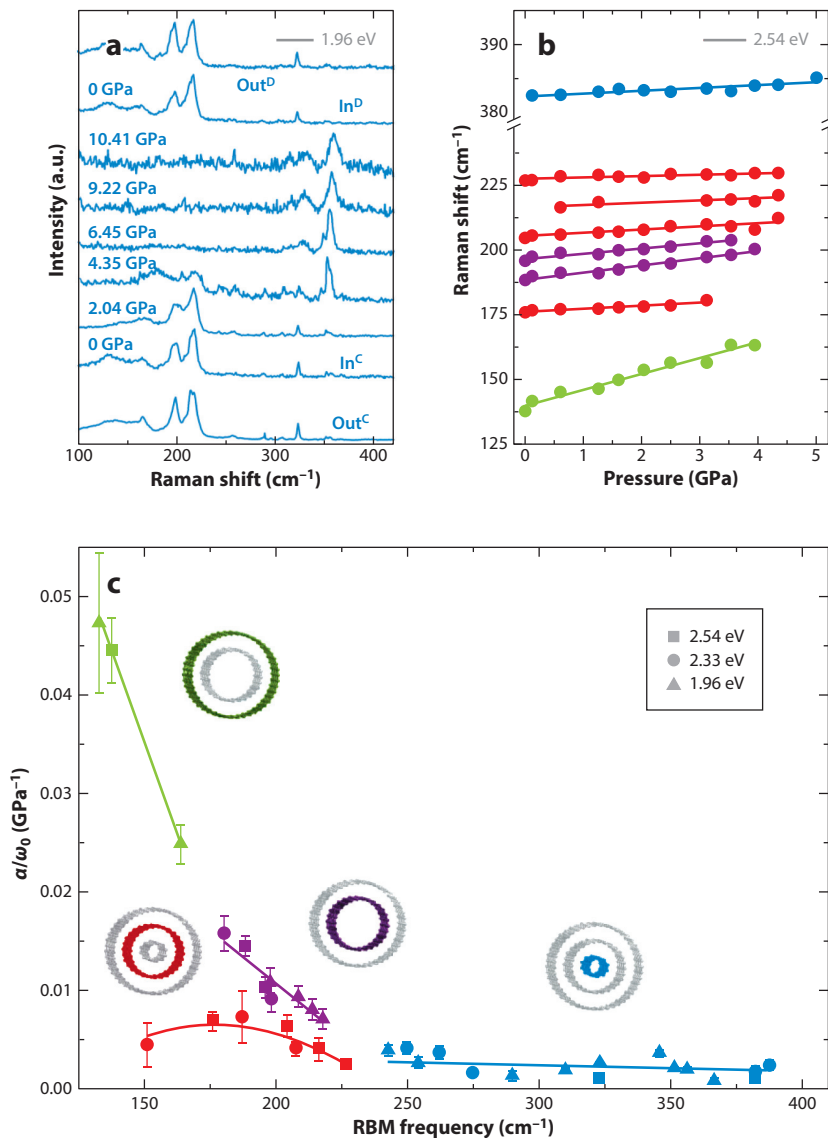
5.2. Triple-Wall Carbon Nanotubes

Similar to the method of producing DWCNTs, TWCNTs have been synthesized from the coalescence of fullerenes encapsulated into DWCNTs (DWCNT peapods) by using thermal treatment in an argon atmosphere or the chemical vapor deposition method (107). The resonance Raman technique was successfully utilized, in both isolated and bundled TWCNTs, for a detailed characterization of the vibrational and electronic properties, the wall-to-wall distances, and the intertube interactions in these carbon nanotube systems (all of which are important due to the high curvature of carbon nanotubes) (108–110). By using resonance Raman spectroscopy together with high-pressure experiments in a sample containing both DWCNTs and TWCNTs, Alencar et al. (111) showed that it is possible to identify the inner tubes in DWCNTs and TWCNTs separately, even if the two tubes have the same diameters, as explained below.

Figure 5a shows the RBM Raman spectra of TWCNTs in bundles at different pressures. For comparison, the ambient-pressure Raman spectra for the TWCNTs outside (before and after pressure loading) and inside the pressure cell are shown. Comparison of the spectra before (lower trace) and after (upper trace) the pressure cycle reveals that the Raman spectra are quite similar, thus indicating that the structural transformations of the tubes due to external pressure are reversible (at least up to 10.4 GPa). The Raman peaks localized above 300 cm^{-1}, attributed to the innermost tubes of the TWCNTs, increase in intensity as the pressure increases. In general, the RBMs of SWCNTs disappear at pressures much lower than 10 GPa, and the result observed for the innermost nanotube of the TWCNTs is due to (a) the shielding provided by the outer shells and (b) a resonance effect induced by pressure, whereby the electronic transition energies of the innermost nanotubes shift and match the photon energy used to excite the spectra (111).

Most of the samples containing TWCNTs also have DWCNTs as impurities, and the diameter distributions of these DWCNTs and TWCNTs are very close to each other. Therefore, when only the RBM spectra are measured, it is difficult to distinguish the origin of the peaks, to determine whether the peaks are related to the intermediate-diameter tube of the TWCNTs, or to determine whether the signal is coming from the innermost tube of the DWCNTs. The ω_{RBM} is a linear function of pressure, and the data can be fitted using $\omega(P) = \omega_0 + \alpha P$. However, when one is normalizing the pressure coefficients α for each spectral line shown in Figure 5b, using the value of the frequency intercept ω_0, and plotting these data versus the initial frequencies generated, it is possible to identify the origin of each RBM with each layer, as shown in Figure 5c. The observed behavior is related to the structural support that the innermost tube provides to the intermediate tube of the TWCNTs, which prevents their deformation and decreases their pressure coefficients (56, 101, 103). Such mechanical support does not occur for DWCNTs, which are more susceptible to larger deformations than are TWCNTs.
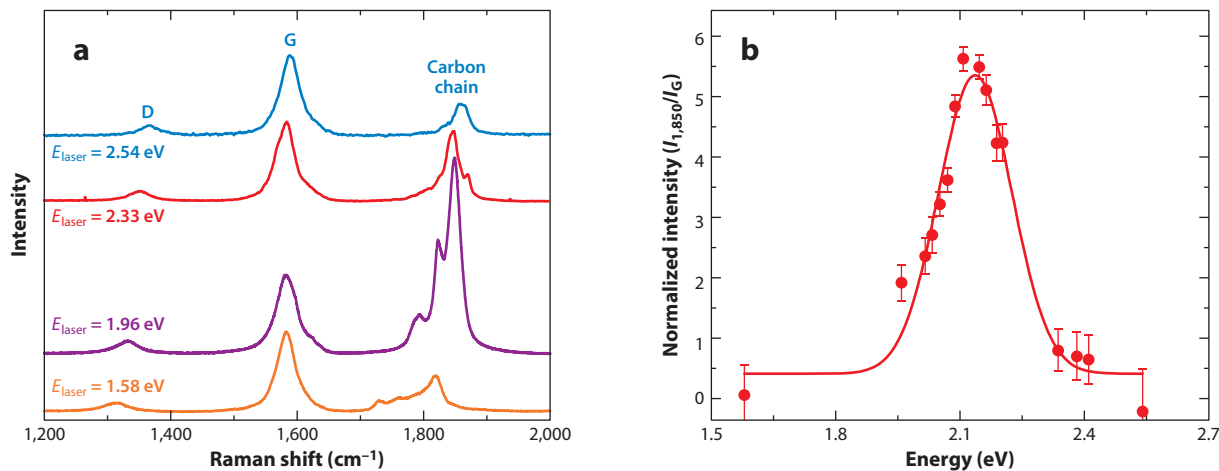
5.3. Linear Carbon Chains

Linear carbon chains, or carbyne, can be considered to be truly one-dimensional solids because they achieve the ultimate one-atom-thick limit. Carbynes are an interesting system because they

Figure 5

(*a*) Evolution of the Raman spectra of triple-wall carbon nanotubes (TWCNTs) with pressure, measured with the laser excitation energy $E_{laser} = 1.96$ eV. The two lowest spectra in panel *a* refer to ambient pressure outside the pressure cell (Out^C) and inside the pressure cell at 0 GPa (In^C), before compression. The two uppermost spectra are for samples inside the pressure cell at 0 GPa (In^D) and at ambient pressure outside the pressure cell (Out^D), after the complete release of pressure. (*b*) The ω_{RBM}-versus-pressure plot obtained for the Raman spectra excited with $E_{laser} = 2.54$ eV (RBM denotes radial breathing mode). The line shapes are obtained from the data taken with three different E_{laser} measurements by using Lorentzian components, and the pressure evolution of each mode was well described by a linear function (56, 60, 61, 98–101).
(*c*) Normalized pressure coefficients ($\frac{\alpha}{\omega_0} = \frac{1}{\omega_0}\frac{d\omega}{dp}$) plotted as a function of ω_{RBM} allow the contributions of each tube type to be separated. In the plot, each point represents an RBM peak at ambient pressure, which is related to a specific tube, whereas the solid lines are guides for the eyes. The innermost tubes of TWCNTs are in blue, the intermediate tubes of TWCNTs are in red, the inner tubes of double-wall carbon nanotubes (DWCNTs) are in purple, and the outer tubes of DWCNTs are in green. Adapted from Reference 111.

Figure 6

(*a*) Resonance Raman spectra of linear carbon chains encapsulated in multiwall carbon nanotubes. The D and G band Raman modes from carbon nanotubes are shown along with the bands from the chains. (*b*) Resonance window of a linear carbon chain mode. Adapted with permission from Reference 121.

are predicted to be the stiffest material under tension and because the strain can be used to modulate their electronic conductance (112, 113). Because carbynes are unstable under ambient conditions (114), carbon nanotubes have been used to encapsulate the chains in their inner core (96, 115–117), which has allowed for great progress in measuring and understanding the vibrational and electronic properties of these one-dimensional solids. Carbyne can have either a cumulene ($\cdots C=C=C=C=C \cdots$) or a polyyne ($\cdots C–C\equiv C–C\equiv C \cdots$) bonding scheme. Theoretical calculations predict that the polyyne configuration is less stable than the cumulene configuration because the latter has a degenerate pair of half-filled energy bands, which experiences a Peirels distortion (118, 119). These structures have normal modes active in Raman scattering, appearing at higher frequencies than the G band (approximately 1,850 cm^{-1} in the bottom spectrum in **Figures 1** and **6**).

Because of their unsaturated bonds, linear carbon chains are unstable and are highly reactive (120); the empty space available in the core of a carbon nanotube is a suitable cage for shielding and stabilizing the carbon chain (96, 115–117, 121). However, once the chains are stabilized in the core of the nanotubes, Raman spectroscopy is an appropriate technique for probing the chains, because these chains exhibit a strong resonance Raman effect and the Raman response can be used to experimentally estimate the electronic gap (122). Furthermore, if the chains are encapsulated in DWCNTs, it is also possible to characterize the tubes and analyze their interaction by monitoring the shifting of the Raman modes due to the charge transfer process (115).

Figure 6a shows the Raman spectra of a sample with a carbon chain inside a multiwall carbon nanotube (MWCNT) for different laser lines. Besides the expected D and G modes from the sp^2 lattice of the MWCNT, a very strong peak is observed near 1,850 cm^{-1}, which is assigned to the carbon chain. The intensities and frequencies of the chain modes strongly depend on the laser energy because, for each chain length, there is a different electronic gap. In addition, the chain length has a strong influence on the carbon-carbon bond distance, which in turn affects the phonon frequency. The mean frequency of the vibrational bands from the carbon chains increases as the laser excitation energy increases, and this upshift can be associated with shorter chains whose

carbon-carbon bond strength (if one assumes that the same bonding type applies) is expected to be weaker than for longer ones.

By using different laser lines, the resonance window for the carbon chains was measured, and the result is shown in **Figure 6b** (121). By fitting the experimental data of **Figure 6b** with a Gaussian line profile, the gap was determined as being 2.13 eV. The value of the energy gap of long one-dimensional carbon chains by means of theoretical models is not well resolved, and this value is very sensitive to the calculation method and thus ranges from 0.2 eV to more than 4 eV, although Al-Backri et al. (123) seem to have solved this discrepancy. These authors used a GW many-body approach to calculate the band gap of an infinite carbon chain, and they obtained a value for long chains of $E_{gap} = 2.16$ eV, which is very close to the maximum in the resonance window shown in **Figure 6b**.

The presence of the chains was confirmed by imaging the carbon nanotube cross section with scanning transmission electron microscopy (STEM), which generates images that are a sum of Z contrast and diffraction contrast when performed with a high camera length and a high-angle annular dark-field (HAADF) detector, as shown in **Figure 7**. In the annular dark-field mode, the image can be easily interpreted because interference artifacts are absent, and the fringes seen in **Figure 7a–c** are directly assigned to the walls of a MWCNT. In **Figure 7a**, it is possible to observe the carbon nanotube cross section, and in **Figure 7c** we see its center with better resolution. By digital image treatment using the fast Fourier transform technique, the carbon nanotube walls are highlighted by selecting frequencies close to the wall separation distance (approximately 0.34 nm). The tube wall separation is also seen in electron diffraction patterning, whereby an intense signal is measured at 2.9 nm^{-1}. In **Figure 7d**, it is possible to distinguish the carbon chain inside the innermost carbon nanotube that has a diameter of 0.82 nm (121). This diameter is consistent with Raman experiments that observed carbon chains only when the RBMs were observed at approximately 330 cm^{-1}, which correspond to a diameter of approximately 0.71 nm.

High-pressure Raman spectroscopy experiments were performed to probe the carbon chains inside the carbon nanotubes. This extreme-condition technique is suitable for accessing the chains owing to advantages such as the following: (*a*) The Raman signal from long linear carbon chains is very strong due to resonance effects, (*b*) high pressure provides an effective tool for tuning the degree of interaction between the carbon chains and their adjacent carbon nanotube wall, and (*c*) the vibrational frequencies of the carbon-carbon stretching are very sensitive to any structural changes that may occur. With increased pressure, the G band frequency value increases (hardening), whereas the band at approximately 1,850 cm^{-1} downshifts (softening), as shown in **Figure 8a**. Through line shape analysis, a frequency-versus-pressure plot can be drawn, and the results for compression and decompression are shown in **Figure 8b**. A similar plot (not shown in **Figure 8**) built for the G band of nanotubes revealed that the spectrum is completely recovered after the pressure cycle. Conversely, from the plot in **Figure 8b** it can be concluded that the overall spectrum of the chain is not completely recovered, thus suggesting that the pressure cycle has induced some irreversible changes and that the linear carbon chains may have undergone some modification in their structure at high-pressure values. A downshift of approximately 13 cm^{-1} is observed for the highest intense peak of the chain, relative to the initial spectrum measured before the pressure cycle. On the basis of atomistic modeling using reactive molecular dynamics simulations, the irreversibility observed in the Raman spectrum of the carbon chain is attributed to the pressure-induced coalescence of individual chains forming longer chains.
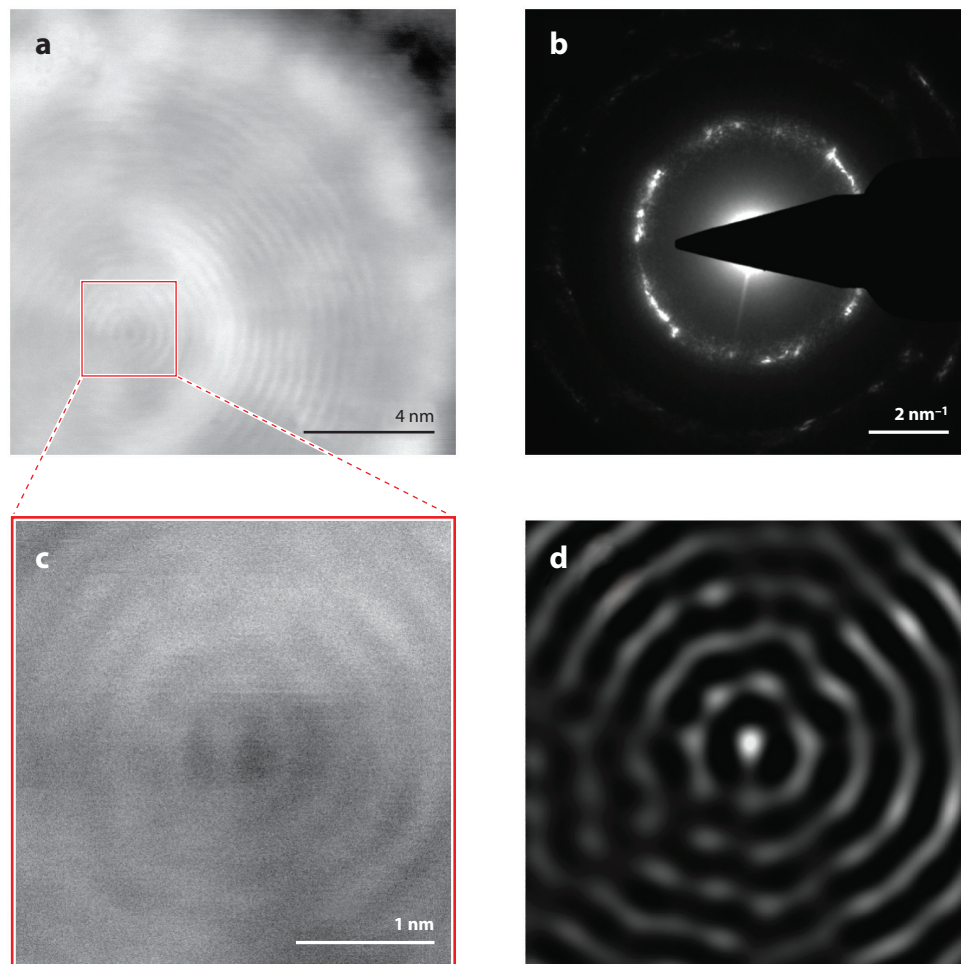
Figure 7

(*a*) Annular dark-field (ADF) image using the scanning transmission electron microscopy (STEM) mode to observe a cross section of a multiwall carbon nanotube (MWCNT) containing a carbon chain in the center. (*b*) Selected-area electron diffraction of a MWCNT cross section. (*c*) An ADF image showing a magnification of the area within the dashed square in panel *a*. (*d*) The same image as in panel *c*, but with image treatment. Frequencies between 2 and 4 nm^{-1} were selected by using a band pass filter (fast Fourier transform) on the image in panel *c*. Adapted with permission from Reference 121.

# 6. PERSPECTIVES: RAMAN SPECTROSCOPY AND CARBON NANOSTRUCTURES FOR DEVELOPING NANOSCIENCE AND NANOTECHNOLOGY

6.1. On the New Phenomena Discussed Here

The richness of Raman spectroscopy as applied to carbon nanostructures is evidenced by the frequent discovery of novel phenomena, related either to the carbon nanostructures or to the experimental tools. Here we discuss some novelties related to the technique—the use of I_{aS}/I_S

Figure 8

(*a*) Raman spectra of
linear carbon chains
encapsulated in
multiwall carbon
nanotubes at different
pressures.
(*b*) Frequency-versus-
pressure plot for the
linear chain modes
during compression
(*solid symbols*) and
decompression (*open
symbols*). Adapted with
permission from
Reference 122.
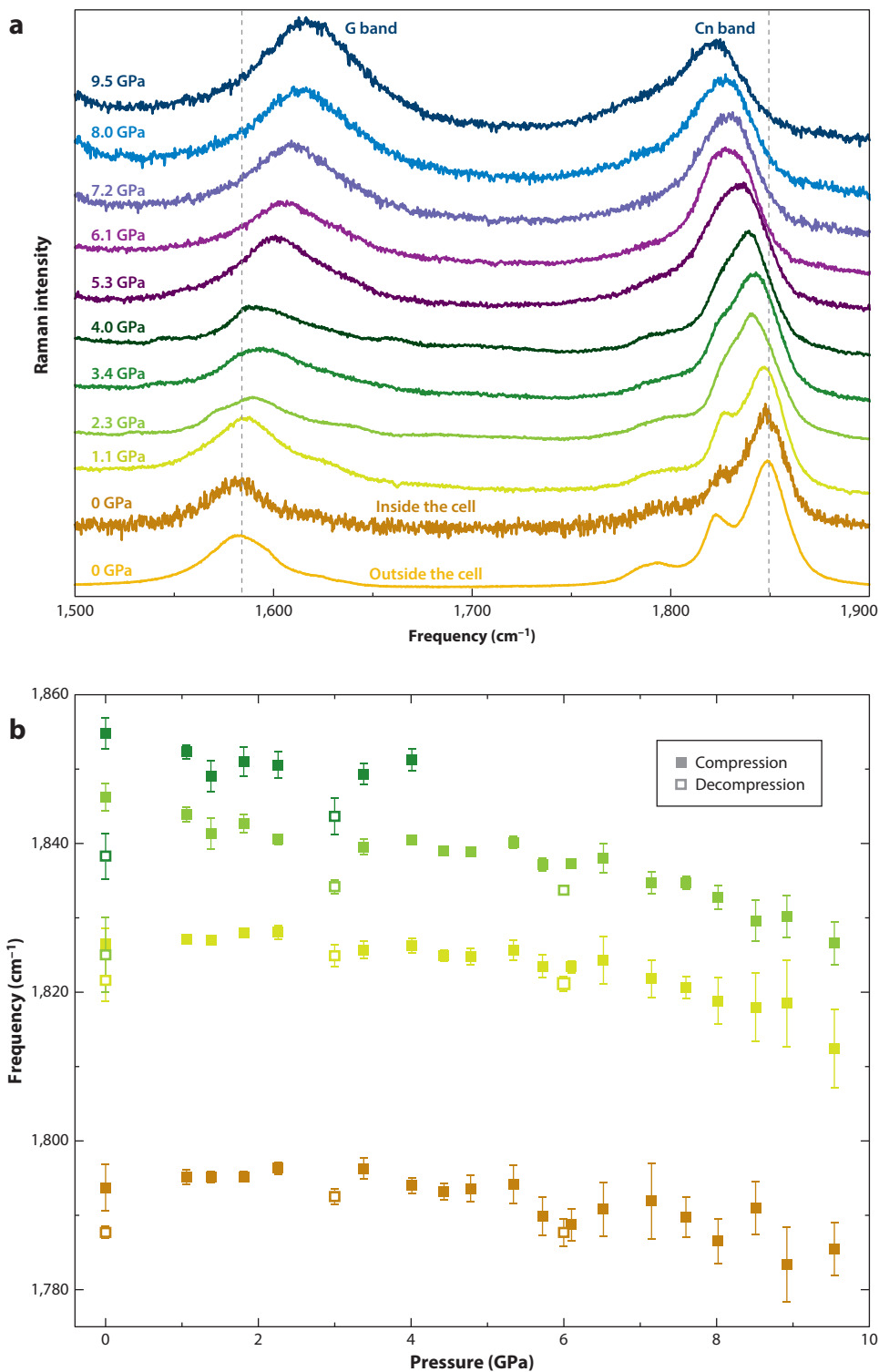
to measure phonon population and the development of TERS—and to the materials, including new findings on the evolution from single- to few-nanotube walls and linear carbon chains inside nanotubes.

6.1.1. Study of Stokes–anti-Stokes correlation.
Dimensionality likely plays a role in enhancing the Stokes–anti-Stokes correlation effect, both through electron and phonon confinement in the reciprocal space, generating van Hove singularities in the density of states, and through real-space confinement of the light-phonon wave functions. Carbon nanotubes exhibit one-dimensional van Hove singularities and strong excitonic effects, which generate strong resonance Raman scattering for both Stokes and anti-Stokes processes (70). Therefore, carbon nanotubes are good candidates for studying the Stokes–anti-Stokes effect. This type of study may shed light on debates related to the origin of asymmetries in the G band resonance profile (124–127).

6.1.2. Development of tip-enhanced Raman spectroscopy.
Carbon nanotubes and graphene have been used as probes for sensing the near-field effects from well-designed plasmonic structures, such as gold dimers (22–24). This approach is generating important developments for the understanding of plasmonic enhancement effects, which are seen not only through TERS, but also through the broadly utilized SERS (surface-enhanced Raman spectroscopy). Another intriguing related effect is GERS (graphene-enhanced Raman spectroscopy), wherein a graphene sheet serves as a substrate for enhancing Raman scattering (128, 129).

From a technique perspective, the unusual TERS findings, with subnanometer resolution (80), are still not fully understood. The reproducibility aspects behind the instrumental implementation of the technique are still unsatisfactory. These are all important directions of research because scanning optical near-field microscopy (SNOM) is expected to play a very important role in materials science.

6.1.3. From single-wall to multiwall carbon nanotubes.
Whereas the differences between graphene and graphite are well understood, the evolution from SWCNT to MWCNT is still poorly described, despite the importance of this evolution for applications. The major reason for this gap in knowledge is the higher complexity of nanotube systems, in which simple AB stacking does not take place. In this sense, DWCNTs, followed by TWCNTs, provide a model system that can be used to understand the properties of carbon nanotubes ranging from SWCNTs to many-layered MWCNTs.

6.1.4. Perfect one-dimensional systems.
Great progress in the study of carbon chains was recently made by preparing ultralong carbynes (as many as 2,300 carbon atoms long) inside DWCNTs (130). The carbon chains inside the DWCNTs were very stable and with high yield, thus moving in the direction of producing bulk carbyne. Electronic band structure calculations have shown that the hybrid system (the chain inside the nanotube) is metallic due to charge transfer from the nanotube to the chain, even if both the nanotube and the chain are semiconducting. Because the carbon chains are very long, all the chains are expected have the same spectrum. Therefore, the multiple Raman peaks observed at approximately 1,850 cm^{-1} have been interpreted as being due to the chains inserted into different nanotubes, as lower-energy phonons are associated with the chains inside lower-diameter carbon nanotubes. Because small-diameter tubes are expected to induce larger strain levels on the chain, the downshift in phonon frequency of the chain is consistent with the high-pressure Raman data that indicate a downshift in carbon-carbon vibrations when the chains are compressed. Furthermore, temperature-dependent data for line widths of the Raman modes showed that the chain and the nanotube are coupled to each other,

and thus the frequency of Raman modes for chains inside nanotubes is approximately 60 cm^{-1} lower than for chains in liquid media (130).

6.2. Applications in Other Fields

This section discusses some fields in which the use of Raman spectroscopy as a characterization tool is promising but still nascent. Important novel results have been published in biotechnology, nanotoxicology, archaeology, and soil sciences, and some results are discussed here.

6.2.1. Biotechnology applications. Researchers are studying different ways of using carbon nanostructures (such as graphene and carbon nanotubes) for developing biotechnological applications. However, a critical issue in this area is the control of purity and dispersion of these nanomaterials in physiological media. To improve dispersion, the nanotubes must be functionalized by using either covalent functionalization (oxidation methods that can lead to graphene oxide or oxidized carbon nanotubes) or noncovalent functionalization (wrapping with polymers). The choice of method is strongly dependent on the application. There are successful protocols for attaining such stable dispersion by using biocompatible polymers, which are promising for their applications in nanomedicine. However, understanding of the mechanisms responsible for colloidal stabilization is not yet clear. Padovani et al. (131) recently reported that the manifestation of a particular mechanism of stabilization of oxidized carbon nanotubes and graphene oxide in the presence of Pluronic F-127 and short- and long-chain polyethylene glycol (PEG) is strongly dependent on proper matching between nanocarbon morphology and polymer chain length, chemical structure, and concentration. The conclusion of Padovani et al. is that, for applications for which the dispersing media has low ionic strengths, the electric stabilization attained by the oxidation of carbon nanomaterials can provide suitable colloidal stability. In contrast, in the particular context of nanomedicine applications—which demand the use of nanocarbons as individualized colloidal entities, and not as agglomerates in physiological media (e.g., 0.9% NaCl, with a high ionic strength)—oxidation-based methods, which lead to electric stabilization through negative surface charging, are not as effective as the use of suitable biocompatible polymers such as Pluronic F-127 and long-chain PEG.

The molecular transporter, in which the carbon nanostructure is used to carry different types of molecules into cells, has also been exploited (18–20). Another largely studied direction is the use of carbon nanotubes for tissue engineering (132); one application is emulating the natural nanostructure of the bone for orthopedic applications (133). In this field, Raman spectroscopy has been used largely to perform spectral imaging to demonstrate the presence of carbon nanotubes inside the target cells (10). Ladeira et al. (19) demonstrated RNA delivery into human and murine cells using MWCNTs, and the G band Raman signal was utilized to prove the presence of the delivery agent, MWCNTs, inside the cells. The MWCNT siRNA delivery system demonstrated nonspecific toxicity and a transfection efficiency greater than 95%.

6.2.2. Nanotoxicology. Many applications of nanomaterials (including nanomaterials based on nanocarbons) are becoming commercially available, and nanotoxicology needs to develop and provide the scientific basis for the safe and sustainable development of nanotechnology in a broad sense. In terms of the regulation and evaluation of hazardous effects, an important step in organizing toxicological information is categorizing or classifying the target materials. Nanomaterials are difficult to classify because they have many parameters such as size, morphology, chemical composition, and materials processing method to take into account. The emerging field of nanotoxicology

is now facing challenges that are not seen in traditional toxicology of molecules. Whereas classical toxicology is based on the dogma of dose concentration response, nanotoxicology depends on dose concentration, size, composition, structure, morphology, surface area, surface charge, and chemical surface groups.

Carbon nanostructures are certainly front-runners in some nanotechnology-based applications because of the richness of new physical phenomena as well as their promising properties to be exploited in real-world applications, and the scientific community must also study these nano-materials from the perspective of safety for both humans and the environment. There are some recent review articles on this subject (134). Metrology protocols for these nanomaterials must be developed before the toxicological effects are investigated. Another key way to advance this field is to understand the various phenomena that emerge at the bio-nano interface. In this context, Raman spectroscopy can contribute to a detailed characterization of the nanomaterials prior to the toxicological assays and to monitoring in situ the interaction of nanocarbons with biological systems. Raman spectroscopy, photoluminescence, and techniques based on an enhanced signal, such as TERS and SERS, will offer sensitive analytical tools by which to measure and correlate the physicochemical properties of carbon nanostructures with the effects that emerge at the bio-nano interface.

6.2.3. Archeology and soil sciences.

There is a broad range of applications for the formula discussed in Section 2.2. One rather unusual example is the study of carbon materials found in the Amazonian rainforest, where ancient Indians subsisted on agriculture in addition to hunting and fishing (10, 13, 135). Although tropical soils are generally unfertile due to high temperatures and heavy rains, the Indians' way of life generated areas of highly fertile soils that were rich in plant nutrients; these areas are known as Amazonian dark earth [in Portuguese, Terra Preta de Índio (TPI)] (12). These anthropogenic Amazonian soils provided a potential model for a sustainable land-use system in the humid tropics, and soil scientists are trying to reproduce the characteristics of such soils by adding charcoal as a soil conditioner to establish whether these soils' recalcitrance and fertility are due to the large concentration of stable sp^2 carbon-based materials.

Equation 3 has been used to characterize different types of biochar found not only in these Amazonian Indian sites, but also in turf, peat, compost, forest deposits, and different types of synthetic charcoals. The analysis demonstrates that TPI has a different crystalline nanostructure (13, 135, 136).

Statistical analysis of the measured Raman spectra from the TPI carbon nanostructures indicates an average crystallite size (L_a) with a general range of $4 < L_a < 9$ nm (**Figure 9a**) (10, 13, 135, 136). The inset to **Figure 9b** shows a Raman spectrum of a TPI carbon sample. Notice the broad D and G Raman lines, characteristic of sp^2 carbon samples with small L_a values. On the basis of this Raman spectroscopy analysis, **Figure 9b** clusters samples of different origins and depths according to L_a. This analysis revealed the formation of two main clusters: The first includes synthetic samples of vegetal charcoal and activated charcoal, and the second includes nonsynthetic samples. Therefore, this Raman spectroscopy–based structural analysis is capable of explaining the differences among black carbon structures from TPI, turf, peat, compost, and nature forest and synthetic vegetal and activated commercial charcoals. However, the properties did not vary significantly between the TPI soil strata (**Figure 9a**) and did not show structural degradation due to the long time permanence in the soil. In contrast, the elemental composition and microbial abundance exhibited a clear depth dependence (136). On the basis of these results, it has been proposed that the nanostructures of the carbon materials found today in the Amazonian sites are similar to the form in which they were produced by the Indians. If this assumption is correct, the key to synthesizing this type of carbon structure is to reproduce the conditions utilized by the
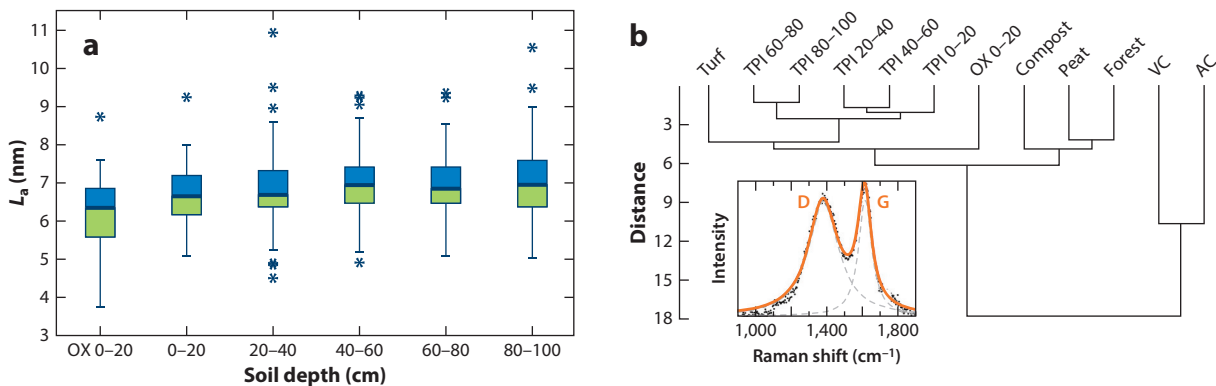
Figure 9

(*a*) Average crystallite size L_a of the carbon nanostructures present in the Terra Preta de Índio as a function of soil depth. OX 0–20 on the *x* axis (*left*) denotes the control soil. For each soil depth range (e.g., 0–20 cm, 20–40 cm, and so forth), the lower boundary of the bottom (*green*) box in the graph denotes the twenty-fifth percentile, and upper boundary of the upper (*blue*) box in the graph denotes the seventy-fifth percentile. The line separating these two boxes denotes the median value. The remaining data are in the range delimited by the horizontal lines outside the boxes, and outliers are represented as asterisks. (*b*) Statistical dendrogram built from the measured values of L_a for the Terra Preta de Índio at different depths and for several other reference samples, as labeled. The inset shows a Raman spectrum of a Terra Preta de Índio sample; the broad D and G Raman lines are labeled. Abbreviations: AC, activated charcoal; OX 0–20, oxisol (at the rain forest, adjacent to the Terra Preta de Índio); TPI, Terra Preta de Índio; VC, synthetic vegetal charcoal. Adapted with permission from Reference 136.

Indians, excluding complex, unknown, long-term soil degradation effects. From materials science, we know that differences in annealing temperature are the main factor that influences L_a and that, by analogy, controlling pyrolysis temperature and atmosphere during residue burning may be a key aspect to reproduce in the application of carbon as a soil conditioner.

DISCLOSURE STATEMENT

The authors are not aware of any affiliations, memberships, funding, or financial holdings that might be perceived as affecting the objectivity of this review.

ACKNOWLEDGMENTS

LITERATURE CITED

1. Dresselhaus MS, Dresselhaus G, Eklund PC. 1996. *Science of Fullerenes and Carbon Nanotubes: Their Properties and Applications*. San Diego: Academic

2. Saito R, Dresselhaus G, Dresselhaus MS. 1998. *Physical Properties of Carbon Nanotubes*. London: Imperial College Press

3. Ferrari AC, Robertson J. 2004. Raman spectroscopy of amorphous, nanostructured, diamond-like carbon, and nanodiamond. *Philos. Trans. R. Soc. A* 362:2477–512

4. Ferrari AC. 2007. Raman spectroscopy of graphene and graphite: disorder, electron–phonon coupling, doping and nonadiabatic effects. *Solid State Commun.* 143:47–57

5. Pimenta M, Dresselhaus G, Dresselhaus MS, Cançado L, Jorio A, Saito R. 2007. Studying disorder in graphite-based systems by Raman spectroscopy. *Phys. Chem. Chem. Phys.* 9:1276–90

6. Reich S, Thomsen C, Maultzsch J. 2008. *Carbon Nanotubes: Basic Concepts and Physical Properties*. Weinheim, Ger.: Wiley-VCH

7. Dresselhaus MS, Jorio A, Hofmann M, Dresselhaus G, Saito R. 2010. Perspectives on carbon nanotubes and graphene Raman spectroscopy. *Nano Lett.* 10:751–58

8. Jorio A, Dresselhaus M, Saito R, Dresselhaus G. 2011. *Raman Spectroscopy in Graphene Related Systems*. Weinheim, Ger.: Wiley-VCH

9. Jorio A. 2012. Raman spectroscopy in graphene-based systems: prototypes for nanoscience and nanometrology. *ISRN Nanotechnol.* 2012:234216

10. Jorio A, Cançado LG. 2012. Perspectives on Raman spectroscopy of graphene-based systems: from the perfect two-dimensional surface to charcoal. *Phys. Chem. Chem. Phys.* 14:15246–56

11. Lucchese MM, Stavale F, Martins Ferreira EH, Vilani C, Moutinho MVO, et al. 2010. Quantifying ion-induced defects and Raman relaxation length in graphene. *Carbon* 48:1592–97

12. Glaser B, Haumaier L, Guggenberger G, Zech W. 2001. The "Terra Preta phenomenon": a model for sustainable agriculture in the humid tropics. *Naturwissenschaften* 88:37–41

13. Ribeiro-Soares J, Cançado L, Falcão N, Martins Ferreira E, Achete C, Jorio A. 2013. The use of Raman spectroscopy to characterize the carbon materials found in Amazonian anthrosoils. *J. Raman Spectrosc.* 44:283–89

14. Mele EJ. 2010. Commensuration and interlayer coherence in twisted bilayer graphene. *Phys. Rev. B* 81:161405

15. Li G, Luican A, Dos Santos JL, Neto AC, Reina A, et al. 2010. Observation of van Hove singularities in twisted graphene layers. *Nat. Phys.* 6:109–13

16. Jorio A, Cançado LG. 2013. Raman spectroscopy of twisted bilayer graphene. *Solid State Commun.* 175:3–12

17. Jorio A, Kasperczyk M, Clark N, Neu E, Maletinsky P, et al. 2014. Optical-phonon resonances with saddle-point excitons in twisted-bilayer graphene. *Nano Lett.* 14:5687–92

18. Liu Z, Winters M, Holodniy M, Dai H. 2007. siRNA delivery into human T cells and primary cells with carbon-nanotube transporters. *Angew. Chem. Int. Ed.* 46:2023–27

19. Ladeira M, Andrade V, Gomes E, Aguiar C, Moraes E, et al. 2010. Highly efficient siRNA delivery system into human and murine cells using single-wall carbon nanotubes. *Nanotechnology* 21:385101

20. Bianco A, Kostarelos K, Prato M. 2005. Applications of carbon nanotubes in drug delivery. *Curr. Opin. Chem. Biol.* 9:674–79

21. Zhao X, Ando Y, Liu Y, Jinno M, Suzuki T. 2003. Carbon nanowire made of a long linear carbon chain inserted inside a multiwalled carbon nanotube. *Phys. Rev. Lett.* 90:187401

22. Schedin F, Lidorikis E, Lombardo A, Kravets VG, Geim AK, et al. 2010. Surface-enhanced Raman spectroscopy of graphene. *ACS Nano* 4:5617–26

23. Heeg S, Fernandez-Garcia R, Oikonomou A, Schedin F, Narula R, et al. 2012. Polarized plasmonic enhancement by Au nanostructures probed through Raman scattering of suspended graphene. *Nano Lett.* 13:301–8

24. Heeg S, Oikonomou A, Fernandez-Garcia R, Lehmann C, Maier SA, et al. 2014. Plasmon-enhanced Raman scattering by carbon nanotubes optically coupled with near-field cavities. *Nano Lett.* 14:1762–68

25. Malard LM, Guimarães MHD, Mafra DL, Mazzoni MSC, Jorio A. 2009. Group-theory analysis of electrons and phonons in N-layer graphene systems. *Phys. Rev. B* 79:125426

26. Piscanec S, Lazzeri M, Robertson J, Ferrari AC, Mauri F. 2007. Optical phonons in carbon nanotubes: Kohn anomalies, Peierls distortions, and dynamic effects. *Phys. Rev. B* 75:1–22

27. Ribeiro-Soares J, Almeida R, Cançado L, Dresselhaus M, Jorio A. 2015. Group theory for structural analysis and lattice vibrations in phosphorene systems. *Phys. Rev. B* 91:205421

28. Tan P, Hu C, Dong J, Shen W, Zhang B. 2001. Polarization properties, high-order Raman spectra, and frequency asymmetry between Stokes and anti-Stokes scattering of Raman modes in a graphite whisker. *Phys. Rev. B* 64:214301

29. Thomsen C, Reich S. 2000. Double resonant Raman scattering in graphite. *Phys. Rev. Lett.* 85:5214–17

30. Ferrari AC, Meyer JC, Scardaci V, Casiraghi C, Lazzeri M, et al. 2006. Raman spectrum of graphene and graphene layers. *Phys. Rev. Lett.* 97:187401

31. Saito R, Jorio A, Souza Filho A, Dresselhaus G, Dresselhaus M, Pimenta M. 2001. Probing phonon dispersion relations of graphite by double resonance Raman scattering. *Phys. Rev. Lett.* 88:027401

32. Tuinstra F, Koenig J. 1970. Raman spectrum of graphite. *J. Chem. Phys.* 53:1126

33. Ferrari AC, Robertson J. 2000. Interpretation of Raman spectra of disordered and amorphous carbon. *Phys. Rev. B* 61:14095–107

34. Tan P, Han W, Zhao W, Wu Z, Chang K, et al. 2012. The shear mode of multilayer graphene. *Nat. Mater.* 11:294–300

35. Lui CH, Malard LM, Kim S, Lantz G, Laverge FE, et al. 2012. Observation of layer-breathing mode vibrations in few-layer graphene through combination Raman scattering. *Nano Lett.* 12:5539–44

36. Popov VN, Van Alsenoy C. 2014. Low-frequency phonons of few-layer graphene within a tight-binding model. *Phys. Rev. B* 90:245429

37. Malard L, Pimenta M, Dresselhaus G, Dresselhaus M. 2009. Raman spectroscopy in graphene. *Phys. Rep.* 473:51–87

38. Gupta AK, Tang Y, Crespi VH, Eklund PC. 2010. Nondispersive Raman D band activated by well-ordered interlayer interactions in rotationally stacked bilayer graphene. *Phys. Rev. B* 82:241406

39. Carozo V, Almeida CM, Ferreira EH, Cancado LG, Achete CA, Jorio A. 2011. Raman signature of graphene superlattices. *Nano Lett.* 11:4527–34

40. Righi A, Costa S, Chacham H, Fantini C, Venezuela P, et al. 2011. Graphene Moiré patterns observed by umklapp double-resonance Raman scattering. *Phys. Rev. B* 84:241409

41. Campos-Delgado J, Cançado LG, Achete CA, Jorio A, Raskin JP. 2013. Raman scattering study of the phonon dispersion in twisted bilayer graphene. *Nano Res.* 6:269–74

42. Takai K, Oga M, Sato H, Enoki T, Ohki Y, et al. 2003. Structure and electronic properties of a non-graphitic disordered carbon system and its heat-treatment effects. *Phys. Rev. B* 67:214202

43. Cançado L, Takai K, Enoki T, Endo M, Kim Y, et al. 2006. General equation for the determination of the crystallite size l_a of nanographite by Raman spectroscopy. *Appl. Phys. Lett.* 88:163106

44. Cançado L, Jorio A, Ferreira E, Stavale F, Achete C, et al. 2011. Quantifying defects in graphene via Raman spectroscopy at different excitation energies. *Nano Lett.* 11:3190–96

45. Ribeiro-Soares J, Oliveros M, Garin C, David M, Martins L, et al. 2015. Structural analysis of polycrystalline graphene systems by Raman spectroscopy. *Carbon* 95:646–52

46. Chou SG, Son H, Kong J, Jorio A, Saito R, et al. 2007. Length characterization of DNA-wrapped carbon nanotubes using Raman spectroscopy. *Appl. Phys. Lett.* 90:131109

47. Martins-Ferreira E, Moutinho M, Stavale F, Lucchese M, Capaz R, et al. 2010. Evolution of the Raman spectra from single-, few-, and many-layer graphene with increasing disorder. *Phys. Rev. B* 82:125429

48. Barros EB, Jorio A, Samsonidze GG, Capaz RB, Souza Filho AG, et al. 2006. Review on the symmetry-related properties of carbon nanotubes. *Phys. Rep.* 431:261–302

49. Spataru CD, Ismail-Beigi S, Benedict LX, Louie SG. 2004. Excitonic effects and optical spectra of single-walled carbon nanotubes. *Phys. Rev. Lett.* 92:077402

50. Milnera M, Kürti J, Hulman M, Kuzmany H. 2000. Periodic resonance excitation and intertube interaction from quasicontinuous distributed helicities in single-wall carbon nanotubes. *Phys. Rev. Lett.* 84:1324–27

51. Fantini C, Jorio A, Souza M, Strano M, Dresselhaus M, Pimenta M. 2004. Optical transition energies for carbon nanotubes from resonant Raman spectroscopy: environment and temperature effects. *Phys. Rev. Lett.* 93:147406

52. Telg H, Maultzsch J, Reich S, Hennrich F, Thomsen C. 2004. Chirality distribution and transition energies of carbon nanotubes. *Phys. Rev. Lett.* 93:177401

53. Jorio A, Saito R, Hafner J, Lieber C, Hunter M, et al. 2001. Structural (*n*, *m*) determination of isolated single-wall carbon nanotubes by resonant Raman scattering. *Phys. Rev. Lett.* 86:1118

54. Araujo P, Pesce P, Dresselhaus M, Sato K, Saito R, Jorio A. 2010. Resonance Raman spectroscopy of the radial breathing modes in carbon nanotubes. *Physica E* 42:1251–61

55. Sasaki K, Saito R, Dresselhaus G, Dresselhaus MS, Farhat H, Kong J. 2008. Curvature induced optical phonon frequency shift in metallic carbon nanotubes. *Phys. Rev. B* 77:245441

56. Christofilos D, Arvanitidis J, Kourouklis GA, Ves S, Takenobu T, et al. 2007. Identification of inner and outer shells of double-wall carbon nanotubes using high pressure Raman spectroscopy. *Phys. Rev. B* 76:113402

57. Caillier C, Machon D, San-Miguel A, Arenal R, Montagnac G, et al. 2008. Probing high-pressure properties of single-wall carbon nanotubes through fullerene encapsulation. *Phys. Rev. B* 77:125418

58. Peters MJ, McNeil LE, Lu JP, Kahn D. 2000. Structural phase transition in carbon nanotube bundles under pressure. *Phys. Rev. B* 61:5939–44

59. Elliott JA, Sandler JK, Windle AH, Young RJ, Shaffer MS. 2004. Collapse of single-wall carbon nanotubes is diameter dependent. *Phys. Rev. Lett.* 92:095501

60. Yao M, Wang Z, Liu B, Zou Y, Yu S, et al. 2008. Raman signature to identify the structural transition of single-wall carbon nanotubes under high pressure. *Phys. Rev. B* 78:205411

61. Capaz RB, Sparatu CD, Tangney P, Cohen ML, Louie SG. 2004. Hydrostatic pressure effects on the structural and electronic properties of carbon nanotubes. *Phys. Status Solid. B* 241:3352–59

62. Ye X, Sun DY, Gong XG. 2005. Pressure-induced structural transition of double-walled carbon nanotubes. *Phys. Rev. B* 72:035454

63. Kürti J, Zólyomi V, Grüneis A, Kuzmany H. 2002. Double resonant Raman phenomena enhanced by van Hove singularities in single-wall carbon nanotubes. *Phys. Rev. B* 65:165433

64. Araujo PT, Maciel IO, Pesce PBC, Pimenta Ma, Doorn SK, et al. 2008. Nature of the constant factor in the relation between radial breathing mode frequency and tube diameter for single-wall carbon nanotubes. *Phys. Rev. B* 77:2–5

65. Dresselhaus M, Jorio A, Saito R. 2010. Characterizing graphene, graphite, and carbon nanotubes by Raman spectroscopy. *Annu. Rev. Condens. Matter Phys.* 1:89–108

66. Jorio A, Lucchese M, Stavale F, Martins-Ferreira E, Moutinho M, et al. 2010. Raman study of ion-induced defects in N-layer graphene. *J. Phys. Condens. Matter* 22:334204

67. Faugeras C, Faugeras B, Orlita M, Potemski M, Nair RR, Geim A. 2010. Thermal conductivity of graphene in corbino membrane geometry. *ACS Nano* 4:1889–92

68. Berciaud S, Han MY, Mak KF, Brus LE, Kim P, Heinz TF. 2010. Electron and optical phonon temperatures in electrically biased graphene. *Phys. Rev. Lett.* 104:227401

69. Steiner M, Freitag M, Perebeinos V, Tsang JC, Small JP, et al. 2009. Phonon populations and electrical power dissipation in carbon nanotube transistors. *Nature Nanotechnol.* 4:320–24

70. Souza Filho A, Jorio A, Hafner J, Lieber C, Saito R, et al. 2001. Electronic transition energy E_{ii} for an isolated (*n*, *m*) single-wall carbon nanotube obtained by anti-Stokes/Stokes resonant Raman intensity ratio. *Phys. Rev. B* 63:241404

71. Song D, Wang F, Dukovic G, Zheng M, Semke E, et al. 2008. Direct measurement of the lifetime of optical phonons in single-walled carbon nanotubes. *Phys. Rev. Lett.* 100:225503

72. Klyshko D. 1977. Correlation between the Stokes and anti-Stokes components in inelastic scattering of light. *Sov. J. Quantum Electron.* 7:755

73. Kasperczyk M, Jorio A, Neu E, Maletinsky P, Novotny L. 2015. Stokes–anti-Stokes correlations in diamond. *Opt. Lett.* 40:2393–96

74. Parra-Murillo CA, Santos MF, Monken CH, Jorio A. 2015. Power dependence of Klyshko's Stokes–anti-Stokes correlation in the inelastic scattering of light. arXiv:1503.01518 [cond-mat.mtrl-sci]

75. Jorio A, Kasperczyk M, Clark N, Neu E, Maletinsky P, et al. 2015. Stokes and anti-Stokes Raman spectra of the high-energy C–C stretching modes in graphene and diamond. *Phys. Status Solid. B* 252(11):2380–84

76. Lee K, Sussman B, Sprague M, Michelberger P, Reim K, et al. 2012. Macroscopic non-classical states and terahertz quantum processing in room-temperature diamond. *Nat. Photonics* 6:41–44

77. Cançado LG, Hartschuh A, Novotny L. 2009. Tip-enhanced Raman spectroscopy of carbon nanotubes. *J. Raman Spectrosc.* 40:1420–26

78. Schmid T, Opilik L, Blum C, Zenobi R. 2013. Nanoscale chemical imaging using tip-enhanced Raman spectroscopy: a critical review. *Angew. Chem. Int. Ed.* 52:5940–54

79. Chen C, Hayazawa N, Kawata S. 2014. A 1.7 nm resolution chemical analysis of carbon nanotubes by tip-enhanced Raman imaging in the ambient. *Nat. Commun.* 5:3312

80. Zhang R, Zhang Y, Dong Z, Jiang S, Zhang C, et al. 2013. Chemical mapping of a single molecule by plasmon-enhanced Raman scattering. *Nature* 498:82–86

81. Hartschuh A, Sánchez EJ, Xie XS, Novotny L. 2003. High-resolution near-field Raman microscopy of single-walled carbon nanotubes. *Phys. Rev. Lett.* 90:095503

82. Cançado L, Jorio A, Ismach A, Joselevich E, Hartschuh A, Novotny L. 2009. Mechanism of near-field Raman enhancement in one-dimensional systems. *Phys. Rev. Lett.* 103:186101

83. Anderson N, Hartschuh A, Cronin S, Novotny L. 2005. Nanoscale vibrational analysis of single-walled carbon nanotubes. *J. Am. Chem. Soc.* 127:2533–37

84. Hartschuh A, Qian H, Meixner AJ, Anderson N, Novotny L. 2005. Nanoscale optical imaging of excitons in single-walled carbon nanotubes. *Nano Lett.* 5:2310–13

85. Saito Y, Hayazawa N, Kataura H, Murakami T, Tsukagoshi K, et al. 2005. Polarization measurements in tip-enhanced Raman spectroscopy applied to single-walled carbon nanotubes. *Chem. Phys. Lett.* 410:136–41

86. Anderson N, Hartschuh A, Novotny L. 2007. Chirality changes in carbon nanotubes studied with near-field Raman spectroscopy. *Nano Lett.* 7:577–82

87. Maciel I, Anderson N, Pimenta M, Hartschuh A, Qian H, et al. 2008. Electron and phonon renormalization near charged defects in carbon nanotubes. *Nat. Mater.* 7:878–83

88. Qian H, Araujo PT, Georgi C, Gokus T, Hartmann N, et al. 2008. Visualizing the local optical response of semiconducting carbon nanotubes to DNA-wrapping. *Nano Lett.* 8:2706–11

89. Saito Y, Verma P, Masui K, Inouye Y, Kawata S. 2009. Nano-scale analysis of graphene layers by tip-enhanced near-field Raman spectroscopy. *J. Raman Spectrosc.* 40:1434–40

90. Domke KF, Pettinger B. 2009. Tip-enhanced Raman spectroscopy of 6H-SiC with graphene adlayers: selective suppression of E1 modes. *J. Raman Spectrosc.* 40:1427–33

91. Stadler J, Schmid T, Zenobi R. 2010. Nanoscale chemical imaging using top-illumination tip-enhanced Raman spectroscopy. *Nano Lett.* 10:4514–20

92. Su W, Roy D. 2013. Visualizing graphene edges using tip-enhanced Raman spectroscopy. *J. Vac. Sci. Technol. B* 31:041808

93. Beams R, Cançado LG, Jorio A, Vamivakas AN, Novotny L. 2015. Tip-enhanced Raman mapping of local strain in graphene. *Nanotechnology* 26:175702

94. Cançado LG, Beams R, Jorio A, Novotny L. 2014. Theory of spatial coherence in near-field Raman scattering. *Phys. Rev. X* 4:031054

95. Beams R, Cançado LG, Oh SH, Jorio A, Novotny L. 2014. Spatial coherence in near-field Raman scattering. *Phys. Rev. Lett.* 113:186101

96. Zhao X, Ando Y, Liu Y, Jinno M, Suzuki T. 2003. Carbon nanowire made of a long linear carbon chain inserted inside a multiwalled carbon nanotube. *Phys. Rev. Lett.* 90:187401

97. Pfeiffer R, Kuzmany H, Kramberger C, Schaman C, Pichler T, et al. 2003. Unusual high degree of unperturbed environment in the interior of single-wall carbon nanotubes. *Phys. Rev. Lett.* 90:225501

98. Ghandour AJ, Dunstan DJ, Sapelkin A, Proctor JE, Halsall MP. 2008. High-pressure Raman response of single-walled carbon nanotubes: effect of the excitation laser energy. *Phys. Rev. B* 78:125420

99. Arvanitidis J, Christofilos D, Papagelis K, Andrikopoulos KS, Takenobu T, et al. 2005. Pressure screening in the interior of primary shells in double-wall carbon nanotubes. *Phys. Rev. B* 71:125404

100. Merlen A, Toulemonde P, Bendiab N, Aouizerat A, et al. 2006. Raman spectroscopy of open-ended single wall carbon nanotubes under pressure: effect of the pressure transmitting medium. *Phys. Status Solid. B* 243:690–99

101. Aguiar AL, Barros EB, Capaz RB, Souza Filho AG, Freire PTC, et al. 2011. Pressure-induced collapse in double-walled carbon nanotubes: chemical and mechanical screening effects. *J. Phys. Chem. C* 115:5378–84

102. Aguiar AL, San-Miguel A, Barros EB, Kalbáč M, Machon D, et al. 2012. Effects of intercalation and inhomogeneous filling on the collapse pressure of double-wall carbon nanotubes. *Phys. Rev. B* 86:195410

103. Puech P, Hubel H, Dunstan DJ, Bacsa RR, Laurent C, Bacsa WS. 2004. Discontinuous tangential stress in double wall carbon nanotubes. *Phys. Rev. Lett.* 93:095506

104. Merlen A, Bendiab N, Toulemonde P, Aouizerat A, Miguel AS, et al. 2005. Resonant Raman spectroscopy of single-wall carbon nanotubes under pressure. *Phys. Rev. B* 72:035409

105. Caillier C, Machon D, San-Miguel A, Arenal R, Montagnac G, et al. 2008. Probing high-pressure properties of single-wall carbon nanotubes through fullerene encapsulation. *Phys. Rev. B* 77:125418

106. Alvarez L, Bantignies JL, Leparc R, Aznar R, Sauvajol JL, et al. 2010. High-pressure behaviour of polyiodides confined into single-walled carbon nanotubes: a Raman study. *Phys. Rev. B* 82:205403

107. Muramatsu H, Shimamoto D, Hayashi T, Kim YA, Terrones M, et al. 2011. Bulk synthesis of narrow diameter and highly crystalline triple-walled carbon nanotubes by coalescing fullerene peapods. *Adv. Mater.* 23:1761–64

108. Hirschmann TC, Araujo PT, Muramatsu H, Zhang X, Nielsch K, et al. 2013. Characterization of bundled and individual triple-walled carbon nanotubes by resonant Raman spectroscopy. *ACS Nano* 7:2381–87

109. Hirschmann TC, Araujo PT, Muramatsu H, Rodriguez-Nieva JF, Seifert M, et al. 2014. Role of intertube interactions in double- and triple-walled carbon nanotubes. *ACS Nano* 8:1330–41

110. Hirschmann TC, Dresselhaus MS, Muramatsu H, Seifert M, Wurstbauer U, et al. 2015. G' band in double- and triple-walled carbon nanotubes: a Raman study. *Phys. Rev. B* 91:075402

111. Alencar RS, Aguiar AL, Paschoal AR, Freire PTC, Kim YA, et al. 2014. Pressure-induced selectivity for probing inner tubes in double- and triple-walled carbon nanotubes: a resonance Raman study. *J. Phys. Chem. C* 118:8153–58

112. Artyukhov VI, Liu M, Yakobson BI. 2014. Mechanically induced metal-insulator transition in carbyne. *Nano Lett.* 14:4224–29

113. Liu M, Artyukhov VI, Lee H, Xu F, Yakobson BI. 2013. Carbyne from first principles: chain of C atoms, a nanorod or a nanorope. *ACS Nano* 7:10075–82

114. Cataldo F. 2006. Polyynes: synthesis, properties, and applications. *J. Am. Chem. Soc.* 128:8987–88

115. Fantini C, Cruz E, Jorio A, Terrones M, Terrones H, et al. 2006. Resonance Raman study of linear carbon chains formed by the heat treatment of double-wall carbon nanotubes. *Phys. Rev. B* 73:193408

116. Nishide D, Dohi H, Wakabayashi T, Nishibori E, Aoyagi S, et al. 2006. Single-wall carbon nanotubes encaging linear chain $C_{10}H_2$ polyyne molecules inside. *Chem. Phys. Lett.* 428:356–60

117. Jinno M, Ando Y, Bandow S, Fan J, Yudasaka M, Iijima S. 2006. Raman scattering study for heat-treated carbon nanotubes: the origin of ≈ 1855 cm^{-1} Raman band. *Chem. Phys. Lett.* 418:109–14

118. Kastner J, Kuzmany H, Kavan L, Dousek FP, Kurti J. 1995. Reductive preparation of carbyne with high yield: an in situ Raman scattering study. *Macromolecules* 28:344–53

119. Yang S, Kertesz M. 2008. Linear CN clusters: Are they acetylenic or cumulenic? *J. Phys. Chem. A* 112:146–51

120. Kertesz M, Yang S. 2009. Energetics of linear carbon chains in one-dimensional restricted environment. *Phys. Chem. Chem. Phys.* 11:425–30

121. Andrade N, Vasconcelos T, Gouvea C, Archanjo B, Achete C, et al. 2015. Linear carbon chains encapsulated in multiwall carbon nanotubes: resonance Raman spectroscopy and transmission electron microscopy studies. *Carbon* 90:172–80

122. Andrade NF, Aguiar AL, Kim YA, Endo M, Freire PTC, et al. 2015. Linear carbon chains under high-pressure conditions. *J. Phys. Chem. C* 119:10669–76

123. Al-Backri A, Zlyomi V, Lambert C. 2014. Electronic properties of linear carbon chains: resolving the controversy. *J. Chem. Phys.* 140:104306

124. Doorn S, Heller D, Barone P, Usrey M, Strano M. 2004. Resonant Raman excitation profiles of individually dispersed single walled carbon nanotubes in solution. *Appl. Phys. A* 78:1147–55

125. Duque JG, Chen H, Swan AK, Shreve AP, Kilina S, et al. 2011. Violation of the Condon approximation in semiconducting carbon nanotubes. *ACS Nano* 5:5233–41

126. Moura L, Moutinho M, Venezuela P, Fantini C, Righi A, et al. 2014. Raman excitation profile of the G band in single-chirality carbon nanotubes. *Phys. Rev. B* 89:035402

127. Hároz EH, Duque JG, Barros EB, Telg H, Simpson JR, et al. 2015. Asymmetric excitation profiles in the resonance Raman response of armchair carbon nanotubes. *Phys. Rev. B* 91:205446

128. Ling X, Zhang J. 2010. First-layer effect in graphene-enhanced Raman scattering. *Small* 6:2020–25

129. Barros E, Dresselhaus M. 2014. Theory of Raman enhancement by two-dimensional materials: applications for graphene-enhanced Raman spectroscopy. *Phys. Rev. B* 90:035443

130. Shi L, Rohringer P, Suenaga K, Niimi Y, Kotakoski J, et al. 2015. Confined linear carbon chains: a route to bulk carbyne. arXiv:1507.04896 [cond-mat.mtrl-sci]

131. Padovani GC, Petry R, Holanda CA, Sousa FA, Saboia VM, et al. 2015. Mechanisms of colloidal stabilization of oxidized nanocarbons in the presence of polymers: obtaining highly stable colloids in physiological media. *J. Phys. Chem. C* 119:18741–52

132. Harrison BS, Atala A. 2007. Carbon nanotube applications for tissue engineering. *Biomaterials* 28:344–53

133. Lahiri D, Ghosh S, Agarwal A. 2012. Carbon nanotube reinforced hydroxyapatite composite for orthopedic application: a review. *Mater. Sci. Eng. C* 32:1727–58

134. Seabra AB, Paula AJ, de Lima R, Alves OL, Durn N. 2014. Nanotoxicity of graphene and graphene oxide. *Chem. Res. Toxicol.* 27:159–68

135. Jorio A, Ribeiro-Soares J, Cançado L, Falcao N, Dos Santos H, et al. 2012. Microscopy and spectroscopy analysis of carbon nanostructures in highly fertile Amazonian anthrosoils. *Soil Tillage Res.* 122:61–66

136. Pagano M, Ribeiro-Soares J, Cançado L, Falcao N, Conçalves V, et al. 2016. Depth dependence of black carbon structure, elemental and microbiological composition in anthropic Amazonian dark soil. *Soil Tillage Res.* 155:298–307

Contents

Index

Errata

An online log of corrections to *Annual Review of Materials Research* articles may be
found at http://www.annualreviews.org/errata/matsci